Received: 1 August 2017 | Revised: 7 May 2018 | Accepted: 20 August 2018

DOI: 10.1002/pip.3075

RESEARCH ARTICLE

WILEY PROGRESS IN PHOTOVOLTAICS

# Comprehensive electrical loss analysis of monolithic interconnected multi-segment laser power converters

Rok Kimovec[1,2] | Henning Helmers[2] | Andreas W. Bett[2] | Marko Topič[1]

[1] Faculty of Electrical Engineering, University of Ljubljana, Tržaška cesta 25, SI-1000 Ljubljana, Slovenia

[2] Fraunhofer Institute for Solar Energy Systems ISE, Heidenhofstr. 2, 79110 Freiburg, Germany

**Correspondence**
Rok Kimovec, University of Ljubljana, Faculty of Electrical Engineering, Tržaška cesta 25, SI-1000 Ljubljana, Slovenia.
Email: rok.kimovec@fe.uni-lj.si

**Funding information**
Slovenian Research Agency, Grant/Award Number: P2-0197

## Abstract

A method for distributed electrical modeling of complete photovoltaic monolithic interconnected modules (MIMs) with complex geometrical and electrical features is developed and applied to study electrical power losses of a six-segment GaAs-based MIM laser power converter (LPC). The model considers spatial dependence of resistive and recombination losses of all epitaxial layers and explicitly takes into account perimeter recombination and the photo-induced leakage current through the semi-insulating GaAs substrate. The investigated specimen was fully parametrized to obtain the model's input parameters which were verified by a comparison of a variety of simulated and measured specimen's electrical characteristics. Based on simulations, we show that distributed series resistance effects, mainly caused by Joule heating in the lateral conduction layer (LCL), limit the efficiency of MIM LPCs under a high irradiance illumination, whereas for a low irradiance illumination perimeter recombination is identified as the limiting factor. Additionally, photo-induced conductivity leads to a reciprocal relationship between irradiance and substrate resistivity, which results in a parasitic shunting between segments and reduces the device efficiency. We present mitigation strategies for the outlined major loss mechanisms and propose a thin-film cell employing a metal back mirror that exploits photon recycling and mitigates LCL losses. With such MIM LPC design, conversion efficiencies above 60% can be reached for a broad irradiance range.

**KEYWORDS**

electrical modeling, laser power converter, lateral conduction layer, monolithic interconnected module, perimeter recombination, photo-induced shunt

## 1 | INTRODUCTION

A monolithic interconnected module (MIM) technology enables to manufacture miniaturized photovoltaic (PV) modules on chip level.[1,2] In such devices, an elevated output voltage on a device level is achieved by a series connection of many electrically separated PV cell segments using standard microelectronic fabrication processing methods.[3] The possibility to increase the output voltage facilitated the use of MIMs in a variety of applications. High voltages and low currents are often required to power micro electro-mechanical systems. Here, an open circuit voltage up to 150 V has been reported for MIMs used to directly power micro electro-mechanical system micro-machined movable mirrors.[4] In thermophotovoltaics, the challenge of low output voltages due to low bandgap single-junction PV cells can be solved by a series connection of individual thermophotovoltaic cell segments in a MIM device.[5] In concentrating PV systems, MIMs can be efficiently employed in dense array receivers used for a high concentrating single dish system.[6] Furthermore, the flexibility to raise the output voltage of MIMs has been successfully exploited to directly power electronic devices in power-over-fiber systems[7-9] in which the light-to-electrical power conversion efficiency in practice exceeds 45%.[8-11] In such galvanically isolated power supplies, monochromatic light of a laser diode is guided through an optical fiber or other non-conductive media to a remote location,

  

where is converted to electricity with a MIM PV device commonly called a laser power converter (LPC).[7-13]

The broad range of applications leads to a variety of geometries (pie-shaped circular,[13] parallel stripes,[3] ...materials [GaAs,[13] InGaAs,[14] Si,[15] ...]) and monolithic interconnection schemes for MIMs.[1] This diversity presents a challenge to establish simulation methods to accurately model and simulate such devices. To some extent and with a given design symmetry, modeling of MIMs can be accomplished with an analytically solvable lumped model.[16] However, to enable modeling of complete MIM devices of arbitrary geometries, a more general approach is required. In this work, we present a method based on a distributed 2.5-dimensional electrical PV two-diode network model; a stack of distributed two-dimensional resistive simulation electrodes vertically interconnected with each other, to form an accurate three-dimensional representation of the device under investigation.

Important modeling parameters of the MIMs are outlined, and one possible solution how to include them in the distributed model is provided in next section. All relevant input parameters for the model of the MIM under investigation—a circular pie-shaped six-segment GaAs LPC—were extracted from a variety of independent measurements on the studied device and test structures manufactured on the same wafer as the investigated specimen, as shown in Section 3. Section 4 details the verification of the model and its input parameters, and based on the simulation results, major loss mechanisms are discussed in light of individual features of the simulated device at various irradiances. Finally, with the obtained findings, we suggest possibilities to reduce major losses and suggest improvements for future devices aiming towards the theoretical conversion efficiency limits of PV devices under monochromatic illumination.[10,17]

## 2 | MIM STRUCTURE AND MODEL DESCRIPTION

### 2.1 | Description of a typical MIM device

The general structure of MIM devices, as shown in Figure 1, does not depend on the end application and exact device geometry.[1] The photoactive and supporting layers of MIM devices, including a thick and highly doped lateral conduction layer (LCL) that provides a low ohmic path for a lateral current flow below the segments, are usually grown with an epitaxial process on an inactive semi-insulating (S.I.) substrate that provides electrical separation of the individual PV cell segments in the finished device.[1] After the epitaxial growth, a first etching step down to the LCL opens the regions where internal electrodes of the individual segments will be contacted and a second etching step into the substrate forms isolation trenches that provide electrical separation of adjacent PV segments. The open etch flanks, namely the perimeter of the *pn*-junction, are coated with a dielectric material to prevent short circuits, and finally, a structured front side metallization provides front and back contact of each segment, the front grid, front and back busbars, as well as serial interconnections between adjacent segments and external contacts in a single processing step.

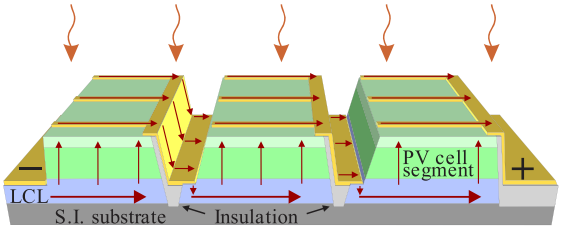


**FIGURE 1** A conceptual drawing of a MIM PV device. Straight red arrows illustrate the current flow through the device. Plus and minus signs on the edges indicate external terminals, both provided on the front side of the device. Note that the lateral current flow towards the grid fingers in emitter and window in MIMs is similar to conventional PV cells [Colour figure can be viewed at wileyonlinelibrary.com]

### 2.2 | Distributed electrical model of MIM devices

The inherently complex geometry and consequently complex current flow in MIMs requires a distributed model to accurately simulate electrical losses. In this work, we developed a distributed electrical model, similar to ones used for conventional solar cells and modules,[18-21] but with explicit features to account for the specifics of the MIMs. The procedure is applied to model a circular small area pie-shaped six-segment MIM GaAs-based PV LPC, which is described in more detail in the following chapter. The model of the complete device was implemented in the open source 2.5-dimensional PV simulation tool PVMOS.[22]

A distributed electrical model consists of a network of numerous elementary units interconnected with resistive grid electrodes through nodes and is able to provide an exact geometrical and functional representation of the modelled device. The role of the individual elementary unit depends on its position in the device. In our case, bulk photoactive areas are modelled with a standard two-diode electrical PV model, whereas non-photoactive elementary units are modelled with resistance. A selection of representative elementary units within simplified representations of the distributed network model is shown in Figure 2.

To preserve the geometrical and electrical complexity of the device, the established distributed numerical model mimics the fabrication of the device. First, a stack of resistive electrodes representing sheet resistances of epitaxial layers (LCL + base, window + emitter) and metallization (front grid and busbars) is defined. Uniquely to this work, a bottom electrode with irradiance-dependent sheet resistance was implemented below the LCL to model a photo induced leakage current through the S.I. substrate, as also observed and discussed in Ohsawa et al and Kimovec et al.[23,24] $r_{S.I.\text{-}GaAs}$ is used as a symbol for this shunting mechanism between adjacent segments, whereas shunting of individual *pn*-junctions ($r_{SH}$) is modeled with a parallel resistance in the two-diode model.

The geometry of the device and roles of elementary units were implemented by using digital images of the photolithographic masks utilized for the manufacturing of the device, shown in Figure 3. In the defined black areas, passive or active connections were established in the model, based on the specific function of that region. Importantly, in mesa regions, all elementary units were replaced with sufficiently high resistors, to avoid computational problems due to undefined

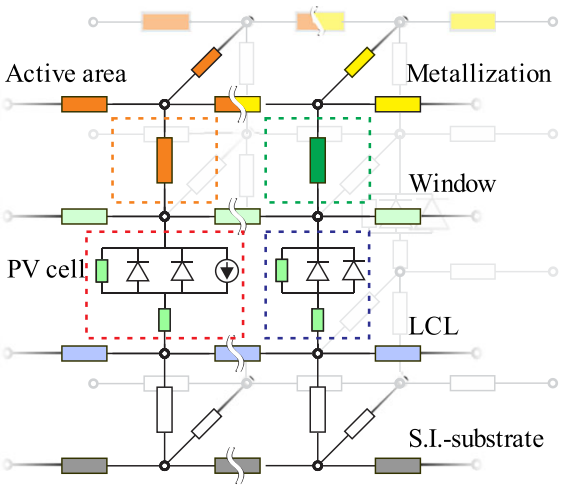


**FIGURE 2** A simplified representation of the used distributed network model. Four representative elementary units of the model are marked with dashed rectangles: The dashed orange box marks unshaded photo-active regions modeled with very high ohmic connections above the window—practically suppressing the current flow, yet still maintaining the simulation nodes for computational reasons. The dark green resistor illustrates the contact resistance between the metal and window simulation electrodes. The window layer is connected to the LCL with a standard two-diode electrical PV model including a series and shunt resistance (dashed red and blue rectangle). The current source representing the photo induced current is omitted where grid fingers and busbars (metallization) shade the *pn*-junction (dashed blue rectangle). Resistive electrodes (planar) connect all elementary units (vertical) to each other through nodes. A bottom electrode with finite sheet resistance is implemented in the model to simulate possible leakage current through the S.I. substrate [Colour figure can be viewed at wileyonlinelibrary.com]

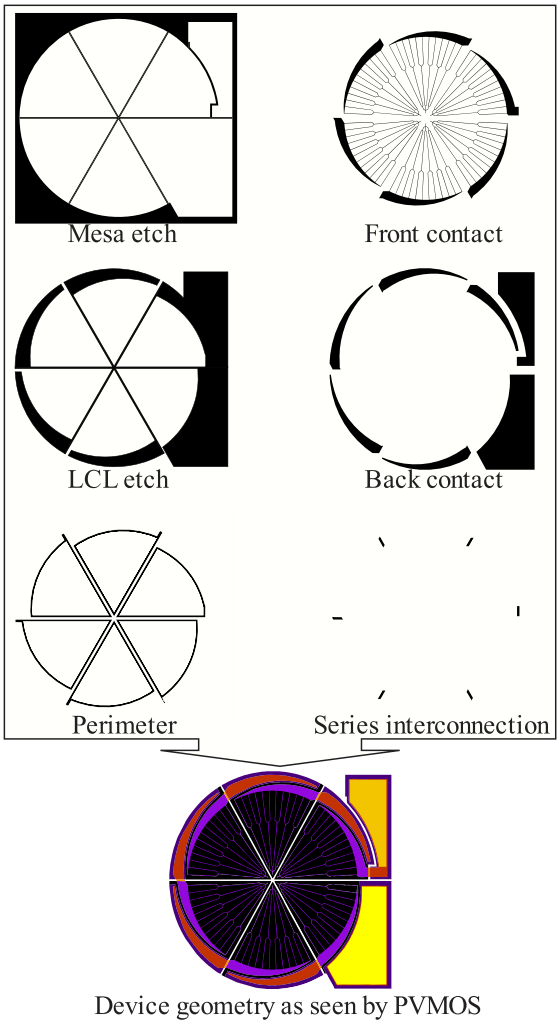


**FIGURE 3** Top: A subset of six modified digital images of photolithographic masks used to define the specimen geometry. Black areas define the specific features in the model. The left column defines the segment geometry (realized through etching in the manufacturing), the right column defines front and back metallization and interconnections between segments (which are all realized in one evaporation step in the manufacturing). Bottom: Top view of the device geometry as seen by PVMOS after implementation. Colors represent the different functional regions of the device (orange: external cathode terminal, yellow: external anode terminal, violet: front grid and cathode busbars, red: back side anode busbars, black: photo-active area) [Colour figure can be viewed at wileyonlinelibrary.com]

boundary conditions but maintain the accuracy of the device geometry. Additional layers in the epitaxial stack (such as barrier layers and tunnel diodes) were considered in the series resistance of the two-diode model elementary units.

To account for perimeter recombination, which is of special importance in small area devices with large perimeter to area ratio,[25] especially when GaAs is used as PV material,[25] dark saturation current density $J_{02}$ was decoupled into two components:

$$J_{02} = J_{02b} + \frac{P}{A} \cdot J_{02p} \tag{1}$$

with $J_{02b}$ being the bulk and $J_{02p}$ the perimeter contribution to $J_{02}$. Consistently, all around the edges of the segments, saturation current, $J_{02}$, was defined as $J_{02p}$, whereas in the bulk $J_{02b}$ was used.

## 3 | STUDIED SPECIMEN

### 3.1 | Sample description

A colored micrograph of the studied six-segment small area MIM LPC is shown in Figure 4. The circular active area of the device has a diameter of 2.08 mm, measured between the busbars, resulting in a designated area of 3.39 mm$^2$. The area of an individual segment is 0.63 mm$^2$ of which 11.1% is covered by a cathode busbar and 7.2% is covered by a metal grid, resulting in an approximately 0.52 mm$^2$ active area per segment exposed to the impinging light. The anode busbars and terminal as wells as the external cathode terminal directly contact the LCL and thus have no *pn*-junction underneath.

Figure 5 shows a conceptual cross-section schematic of the investigated device. The epitaxial layer structure is grown by metalorganic vapor phase epitaxy on a 4″ S.I. GaAs substrate. The structure is based on a GaAs *np*-junction (3650 nm absorber), topped with a 400-nm thick *n*-type GaInP window layer (FSF) which improves the lateral conduction to the metal fingers,[26] and bottomed with a *p*-type GaInP back surface field. To obtain high lateral conductivity below the PV cell layers, a highly doped *n*-type GaAs LCL (5 μm) is used. Consequently,

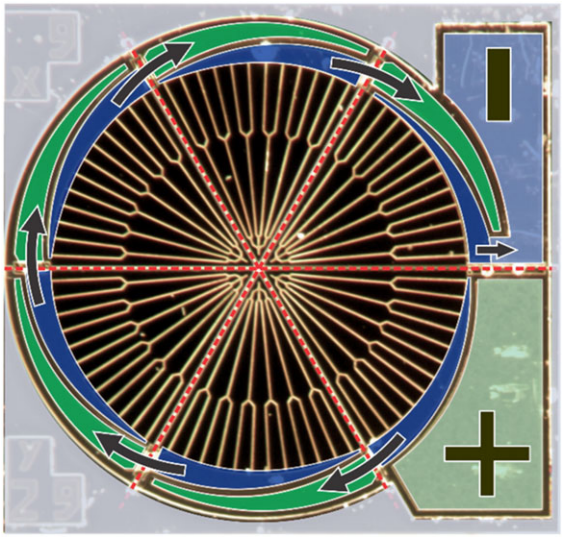

**FIGURE 4** A colored micrograph of the six-segment MIM LPC investigated in this work. Black arrows illustrate the series connections of the segments, and red dashed lines mark the isolation trenches. Dark blue color marks segment cathodes, whereas dark green color marks segment anodes. The remaining inactive area outside the device (mesa area) is greyed out. Plus (light green) and minus (light blue) signs mark the external terminals [Colour figure can be viewed at wileyonlinelibrary.com]

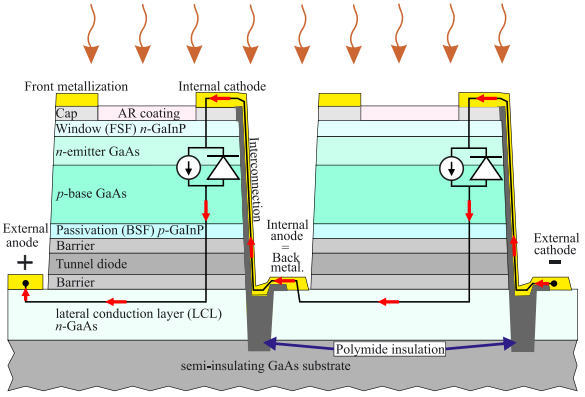


**FIGURE 5** A conceptual cross-section schematic (not to scale) of the investigated MIM LPC, showing the epitaxial layer structure grown on the semi-insulating substrate, and the microstructure that enables monolithic series connection of adjacent segments. A simplified electric circuit is shown, with red arrows illustrating the current path. The resistor symbol illustrates the shunting between segments through the semi-insulating substrate [Colour figure can be viewed at wileyonlinelibrary.com]

a tunnel diode must be incorporated between the *p*-type back surface field and the *n*-type LCL for an ohmic connection between different types of semiconductors. Further, a single scheme low-ohmic semiconductor-metal contact is possible and used by incorporating a *n*-type GaAs cap layer (equally doped as the LCL) above the window. After the epitaxial growth devices are fabricated using micro-structuring photolithographic processes, wet etching, polyimide insulation and evaporation of a metal and a double layer anti-reflection coating.[11]

Further details about the device structure and processing techniques can be found elsewhere.[13]

### 3.2 | Parametrization and numerical representation of the sample

In order to obtain numerical values as input parameters for the model, the specimen was investigated by a variety of independent measurements. The values together with the respective applied extraction method are listed in Table A1 in the appendix. In the following, the most important methodological steps are outlined.

*I-V* measurements under transient illumination were performed using monochromatic diode laser light $\lambda_0$ = 809 nm at various irradiances, utilizing a four-probe measurement technique and a temperature-controlled measuring chuck at 25°C.[27] From the *I-V* measurements and designated segment area, we calculated illuminated current density-voltage curves (*J-V*) plotted in Figure 6.

The dark *I-V* curve plotted in Figure 7 was measured with an Agilent B2901A precision source measurement unit, employing a four-probe measurement technique on a temperature-controlled measuring chuck at 25°C. The dark characteristic was used to extract the diode saturation current density $J_{02}$ with an ideality factor 2, which was decoupled into the bulk component $J_{02b}$ and the perimeter component $J_{02p}$ according to Equation (1).

Additionally, sheet resistances of individual epitaxial layers were measured and extracted from transmission line method[28] measurements on dedicated test structures manufactured on the same wafer as the studied MIM LPC.

## 4 | RESULTS AND DISCUSSION

### 4.1 | Validation and verification of the model

Once the device was fully characterized and the model was built, we performed initial simulations to validate and verify the established

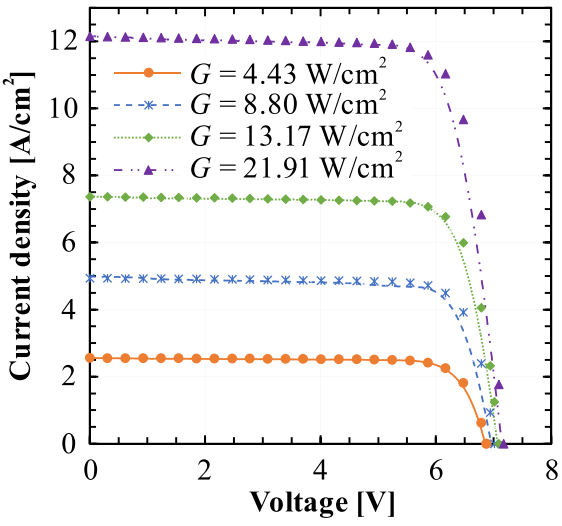


**FIGURE 6** Simulated (symbols) and measured (lines) *J-V* curves at various irradiances *G* of monochromatic light ($\lambda_0$ = 809 nm) for the investigated six-segment MIM LPC [Colour figure can be viewed at wileyonlinelibrary.com]

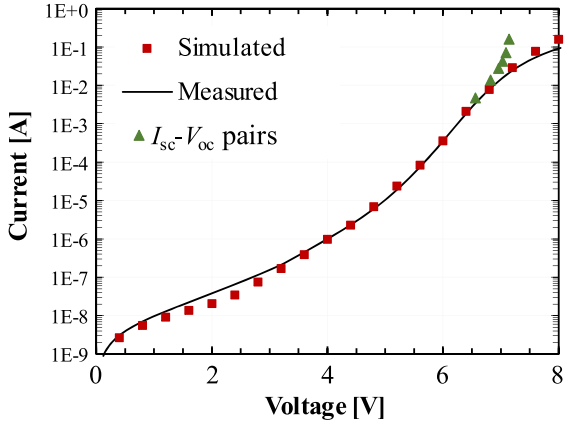


**FIGURE 7** Simulated (squares) and measured (line) dark *J-V* plot of the investigated six-segment MIM LPC. Triangles mark $I_{sc}$-$V_{oc}$ (free of influences from series-resistance) pairs extracted from measured illuminated *I-V* curves at various irradiances [Colour figure can be viewed at wileyonlinelibrary.com]

model and input parameters. This was done by comparing measured illuminated *J-V* curves with simulated illuminated *J-V* curves at various irradiances *G* [W/cm$^2$] (Figure 6) and by comparing the measured dark *I-V* curve with the simulated dark *I-V* curve (Figure 7). For the simulations, the photo-induced current density and the substrate resistivity $r_{S.I.-GaAs}$ are varied with respect to the actual irradiance; all other parameters were kept constant. Good agreement between all simulated and measured curves is observed: The simulated open circuit voltage ($V_{oc}$) deviates ≤0.4%. Regarding the power at the maximum power point ($P_{mpp}$), a small overestimation between 0.2% (for the lowest irradiance) and 2.8% (for the highest presented irradiance) remains.

In addition to the *J-V* curves, which were partly also used to extract the models input parameters, another independent characteristic was used to conclusively verify the model and its input parameters. This was done by comparing measured and simulated spatial electroluminescence (EL) images. The EL measurement of the forward electrically biased specimen ($I_{bias}$ = 10 mA, $V_{bias}$ ≈ 6.8 V) held at an actively controlled temperature of *T* = 25°C[12] was performed with a scientific CCD camera. The simulated EL image was obtained from the spatial map of the junction voltage $V_j$ at the same $I_{bias}$ = 10 mA, $V_{bias}$ ≈ 6.8 V, *T* = 25°C in combination with the reciprocity theorem[29]:

$$EL = const. \cdot e^{\left(\frac{q \cdot V_j}{k \cdot n_{EL} \cdot T} - 1\right)} \quad (2)$$

where kT/q is the thermal voltage and $n_{EL}$ = 2 was calculated from the slope of measured *EL* ($V_{bias}$) characteristic.

The resulting spatial maps and a characteristic line scan from the edge of a segment towards the center of the device are shown in Figure 8. A very good agreement between measured and simulated EL is observed and verifies the developed model and used input parameters. A more detailed analysis of individual features seen in the EL spatial maps can be found in Kimovec et al[30]

## 4.2 | Simulation results

After the validation of the model, we performed a detailed analysis of the individual electrical power loss channels, namely the series resistance, shunt losses, and carrier recombination.

Figure 9 shows the modeled efficiency of the device as a function of monochromatic irradiance considering different scenarios: Yellow circles correspond to the modeled device, i.e., the model with all loss mechanisms included. The investigated six-segment MIM LPC exceeds 52% conversion efficiency at an optimal irradiance of 13.2 W/cm$^2$ and achieves well above 40% conversion efficiency at high irradiances. In addition, the simulated efficiencies are plotted where one dedicated loss channel was switched off, namely series resistance (blue triangles), $r_{S.I.-GaAs}$ (green squares), and perimeter recombination (purple diamonds). From this plot, the dominance of the respective loss mechanism at different irradiances can be clearly observed:

i. At a low irradiance, perimeter recombination significantly limits efficiency. With increasing irradiance, the related losses saturate and become less important since neutral region recombination dominates the recombination losses.
ii. On the contrary, series resistance losses are negligible at low irradiance but increase drastically with increasing irradiance due to their quadratic relationship with the current density: $\Delta P_{Rs} = R_s J^2$.
iii. Interestingly, shunt losses between the segments deteriorate the efficiency independently of irradiance by approximately 1.2% absolute, since the reduced $r_{S.I.-GaAs}$ and irradiance follow a reciprocal relationship.[24]

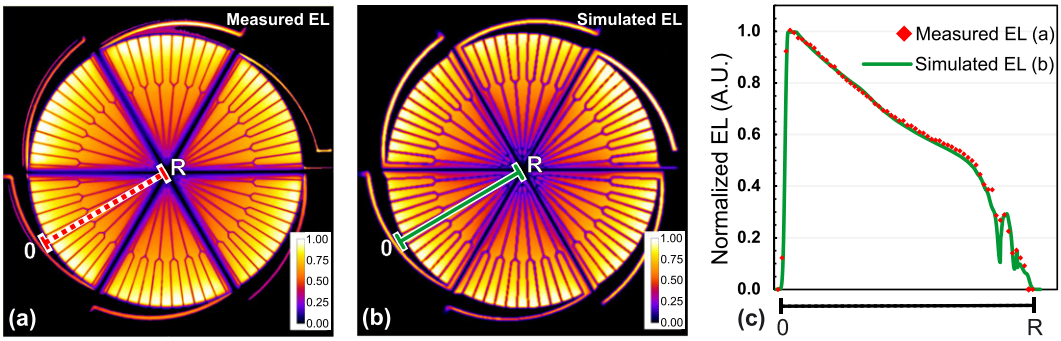


**FIGURE 8** (a) and (b), Measured and simulated normalized EL spatial maps of the studied specimen at forward electrical bias $I_{bias}$ = 10 mA, $V_{bias}$ ≈ 6.8 V and *T* = 25°C. (c), representative line scans of the simulated and measured EL images from the edge (0) towards center (R) [Colour figure can be viewed at wileyonlinelibrary.com]

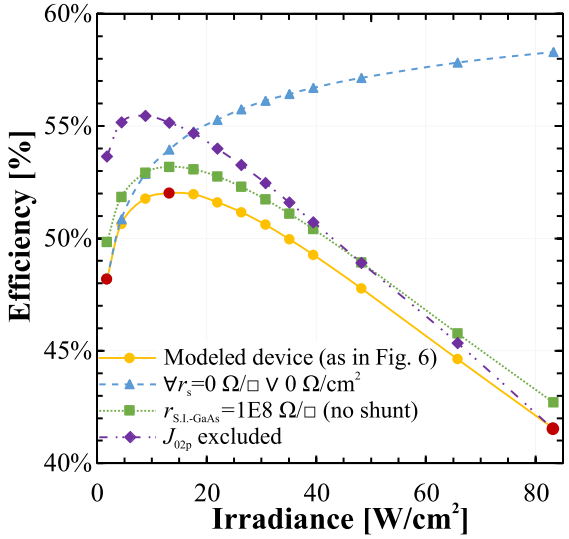


**FIGURE 9** A plot of the modeled efficiency of the investigated sample versus monochromatic irradiance ($\lambda_0$ = 809 nm) (yellow circles) and three different scenarios, where one dedicated resistive loss mechanism is switched off (blue triangles: series resistance, green squares: shunt between segments, purple diamonds: perimeter recombination). Symbols mark simulated data points, whereas lines serve as a visual guideline. Red circles on the yellow curve mark three distinct cases for further analysis [Colour figure can be viewed at wileyonlinelibrary.com]

Finally, it is noteworthy that at the peak efficiency, the performance is influenced by all major loss mechanisms: recombination, resistive, and shunting losses.

In the following three paragraphs, these three power losses are studied for three different irradiance cases ($G_{low}$ = 1.8 W/cm$^2$, $G_{opt}$ = 13.2 W/cm$^2$, $G_{high}$ = 83.1 W/cm$^2$), marked with red circles in Figure 9.

## 4.3 | Joule and shunting losses—Resistive power losses

To analyze the relative contribution of an individual loss component to the total resistive power losses consisting of Joule heating ($r_{BUSBAR}$, $r_{FINGERS}$, $r_{CONTACT}$, $r_{WINDOW}$, $r_{VERTICAL}$, $r_{LCL}$) and shunting ($r_{S.I.\text{-}GaAs}$, $r_{SH}$), the validated model was adapted as follows: recombination parameters were set to the values stated in Table A1 and $r_{S.I.\text{-}GaAs}$ was set to the value of $r_{S.I.\text{-}GaAs\text{-}dark}$, while $r_{SH}$ was omitted from the two-diode model and all series resistances were set to zero. This served as the best-case scenario ("reference case") where all electrical losses were caused solely by recombination losses.

Electrical power losses at the maximum power point ($P_{mpp}$) of the individual resistive loss component were obtained by setting the individual resistance parameters to their measured values one-by-one. A summary of the results for three distinct irradiance cases is listed in Table A2 in the appendix, and the relative contribution of an individual resistive loss mechanism to the overall resistive power losses for three distinct irradiances is illustrated in Figure 10.

From Figure 10, it can be seen that the significance of the different resistive components varies with irradiance:

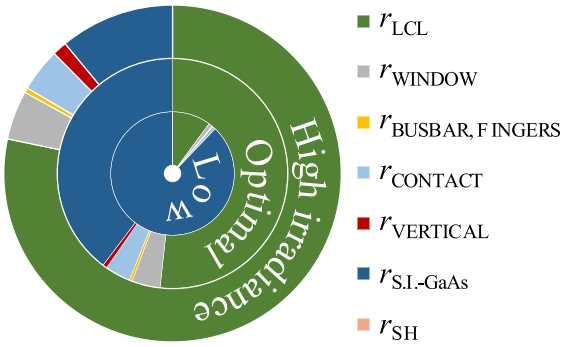


**FIGURE 10** A relative contribution of the individual resistive loss mechanism to the total resistive power losses for three different irradiances: $G_{low}$ = 1.8 W/cm$^2$, $G_{optimal}$ = 13.2 W/cm$^2$, and $G_{high}$ = 83.1 W/cm$^2$ [Colour figure can be viewed at wileyonlinelibrary.com]

i. Basically, all shunting losses originate from the photo-induced leakage current through the S.I. substrate ($r_{S.I.\text{-}GaAs}$). The influence from shunting of individual junctions ($r_{SH}$) can be neglected.

ii. At low irradiance, the resistive power losses due to the combined Joule heating are small (12%) and the majority of the resistive power losses originates from the photo-induced shunting between the segments.

iii. At optimal irradiance, the relative contribution of $r_{S.I.\text{-}GaAs}$ on the resistive power losses is strongly reduced, and the Joule heating due to the current flow in the LCL becomes the dominant resistive loss mechanism.

iv. At high irradiance, this is even more pronounced, where more than 78% of the resistive power losses are caused by the Joule heating in the LCL. The contributions of the losses due to the lateral current flow in the top layers ($r_{WINDOW}$ + $r_{BUSBAR}$ + $r_{FINGERS}$ + $r_{CONTACT}$ $\triangleq$ 10%) also become more pronounced, whereas a relative loss due to $r_{S.I.\text{-}GaAs}$ is significantly reduced.

## 4.4 | Recombination power losses

Power losses related to recombination were analyzed in comparison with a practically achievable "best" case, defined by diode saturation currents $J_{01}$ and $J_{02}$ of state-of-the-art GaAs PV cells ($J_{01}$ = 3E − 20 A/cm$^2$, $J_{02b}$ = 2E − 11 A/cm$^2$ [18]) while omitting perimeter recombination, which provided us with the "reference case." In analogy to the resistive loss analysis, all other parameters were set to their nominal values according to Table A1 and the resulting distribution of recombination losses is summarized in Table A3.

In analogy with Figure 8, Figure 11 shows the influence of the investigated changes in recombination losses on the efficiency as a function of irradiance.

(i) The bottommost yellow circles again show the specimen efficiency obtained with the validated model.

(ii) Reduction of $J_{01}$ from 5E − 20 A/cm$^2$ (measured value of investigated device) to 3E − 20 A/cm$^2$ (state-of-the-art GaAs value; orange triangles) leads to a slight improvement only at the highest studied

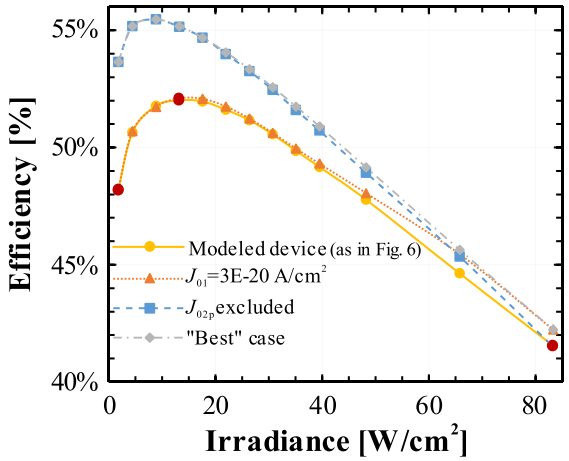


**FIGURE 11** Simulated efficiencies versus monochromatic irradiance ($\lambda_0$ = 809 nm) of the specimen obtained with the validated model (yellow circles) and for three different scenarios, where dedicated recombination mechanisms are improved individually; orange triangle: "best" case $J_{01}$ with included $J_{02p}$; blue squares: "nominal" $J_{01}$ without perimeter recombination; grey diamond: "best" case $J_{01}$ and $J_{02b}$ and excluded $J_{02p}$ = "best" case. Symbols mark simulated data points, whereas lines serve as visual guides. Red circles on the yellow curve mark three distinct irradiance cases for the results summarized in Table A3 in the appendix [Colour figure can be viewed at wileyonlinelibrary.com]

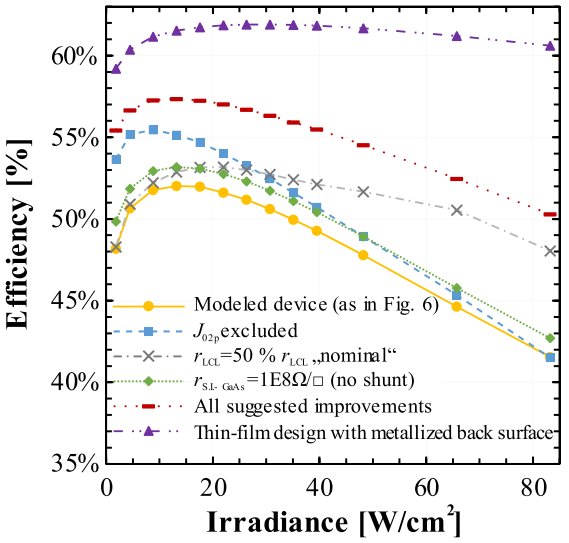


**FIGURE 12** Efficiency potential of the proposed improvements for the investigated six-segment pie-shaped MIM LPC. Blue squares, grey crosses, and green diamonds correspond to improved individual device features; red dashes present a device with all these changes included (compare text). Purple triangles correspond to a thin-film inverted grown device with a back side metallization for a lateral conduction and with an implemented back mirror. Marks correspond to simulated data while lines serve only as a visual guide [Colour figure can be viewed at wileyonlinelibrary.com]

irradiances. Nevertheless, at such high irradiances, efficiency is severely dominated by resistive losses and the improvement of $J_{01}$ is of minor importance.

(iii) Most importantly, a proper passivation of the perimeter (blue squares) results in a significant efficiency boost at low and medium irradiances, while the peak efficiency shifts to lower irradiance. Passivation of the *pn*-junction edges would lead to a 3.5% absolute increase of the efficiency at optimal irradiance.

(iv) The combination of both improvements ($J_{02p}$ excluded + $J_{01}$ = 3E-20 A/cm$^2$ = "best" case values; grey diamonds) results in elevated efficiency for all studied irradiances.

## 5 | POSSIBLE IMPROVEMENTS

The performed analysis reveals several options to improve MIM LPCs performance:

i. At low and medium irradiances, the device could gain up to 5% (relative) in efficiency by effective perimeter passivation, namely at the mesa edges as shown with blue squares in Figure 12. As recently proposed, this could possibly be implemented by a chemical treatment with trioctylphosphine sulfide as a good method for passivating mesa edges in small area GaAs PV cells.[31]

ii. At high irradiances, reduction of the sheet resistance of the LCL $r_{LCL}$ results in the largest improvement of the device performance. A reduction of $r_{LCL}$ by 50% (grey crosses in Figure 12) would result in a 14% relative performance gain at the irradiance 83.1 W/cm$^2$. However, this requires doubling the LCL thickness.

iii. Effective suppression of the photo-induced leakage current in the S.I. GaAs substrate, either by implementing reverse biased diodes between the LCL and the substrate or by preventing the impinged light reaching the substrate altogether, would result in up to a 1.2% absolute gain in efficiency over all investigated irradiances (green diamonds in Figure 12).

iv. All proposed changes together (red dashes in Figure 12) would result in a device with a peak efficiency of 57% (at irradiance 13.2 W/cm$^2$) which presents a 5% absolute increase of the peak efficiency compared with the investigated device. Furthermore, the efficiency drop with increasing irradiance would be reduced.

v. Further improvements can be envisioned by more drastic changes in the design and manufacturing processes. One such approach is to realize an inverted grown thin-film design, as presented in Dentai et al.[32] Thin-film processing enables us to access the back surface of the device, enabling back surface metallization of each segment to improve lateral conduction and consequently mitigate LCL-related losses. At the same time, a back mirror could be implemented to exploit the benefits of photon recycling.[33,34]

To simulate such a device and predict its efficiency potential, the developed model was adapted as follows:

- the $r_{LCL}$ was set to the $r_{BUSBAR}$ value,
- an additional contact resistance between the base and back metallization was introduced,

- since there is no need for a S.I. substrate in such devices, it was excluded from the model
- diode parameters were taken from state-of-the-art thin-film GaAs PV cells with a back mirror, exploiting photon recycling effects ($J_{01}$ = 6E − 21 A/cm$^2$, $J_{02b}$ = 1E − 12 A/cm$^2$ [35]) and
- perimeter recombination was excluded from the model.

The resulting efficiency curve is plotted with purple triangles in Figure 12. Such a device has the potential to achieve conversion efficiencies above 60% over a broad range of monochromatic irradiances (5-85 W/cm$^2$), with the peak efficiency of almost 62% at an irradiance 31 W/cm$^2$.

## 6 | SUMMARY AND CONCLUSION

We developed a validated electrical model of a six-segment small area MIM LPC based on a distributed numerical approach, which takes into account all relevant electrical loss mechanisms, namely sheet resistances of various semiconductor epitaxial layers, the sheet resistance of the metallization, and the recombination losses. In contrast to previous studies, perimeter recombination and photo-induced leakage current through the S.I. substrate were specifically taken into account at the places of their origins. The complex geometry of a whole device was implemented in the model, based on a procedure that allows for easy adaptation to implement also other arbitrary geometries and further enables simple inclusion of localized loss mechanisms.

All relevant input parameters for the model were obtained with a variety of independent measurements, and the validity of the model was confirmed by comparing simulated and measured illuminated *J-V* curves and the dark *I-V* curve at various irradiances. Furthermore, an accuracy of the used input parameters and the established model was verified by comparing simulated and measured EL spatial maps and their characteristic line scans.

The conversion efficiency of the investigated six-segment MIM LPC is over 40% for all studied irradiances (1.8 to 83.1 W/cm$^2$) under homogeneous monochromatic ($\lambda_0$ = 809 nm) illumination and at an optimal irradiance of 13.2 W/cm$^2$ the conversion efficiency of the specimen exceeds 52%. To further improve the performance of such devices, a detailed electrical loss analysis was carried out to find the most significant loss mechanisms. We found that at low monochromatic ($\lambda_0$ = 809 nm) irradiance (1.8 W/cm$^2$), mainly perimeter recombination and leakage through the S.I. GaAs substrate limit the performance of the device. The latter reduces the efficiency by approximately 1.2%$_{abs.}$ regardless of the irradiance, due to a reciprocal relationship between the irradiance and the resistivity of the S.I. GaAs substrate.[23] At high irradiance (83.1 W/cm$^2$), efficiency is limited by series resistance losses, most significantly due to the Joule heating in the LCL. Furthermore, only at very high irradiance illumination, perimeter recombination losses saturate, and recombination losses are dominated by bulk recombination.

In summary, the presented model allows for a quantitative analysis of how different loss mechanisms deteriorate the performance of the specimen under investigation. Additionally, qualitative assessments of the most deteriorating loss mechanisms presented in this work offer systematic improvements of similar small area MIM devices. As an example, for the considered geometry, peak efficiency of up to 57% at optimal irradiance 13.2 W/cm$^2$ can be reached by implementation of minor changes to the design, manufacturing, and processing steps. Notably, a significant improvement of the MIMs' performance is realistically only possible by rather drastic changes in the manufacturing and processing steps, namely implementing a thin-film inverted grown device that exploits photon recycling and mitigates LCL losses by implementing a metal back sheet. It is shown that such a device exhibits an efficiency potential of above 60%.

## ACKNOWLEDGEMENTS

The authors thank Kasimir Reichmuth for fruitful discussions and Ian A. Mihailović for proofreading the manuscript. R.K. thanks Bart Pieters, author of the PVMOS tool, for the support regarding the simulation tool used in this work. The authors acknowledge the financial support from the Slovenian Research Agency (program P2-0197 and PhD funding for R.K.).

## ORCID

*Rok Kimovec* http://orcid.org/0000-0001-9125-9162
*Henning Helmers* http://orcid.org/0000-0003-1660-7651

## REFERENCES

1. Datas A, Linares PG. Monolithic interconnected modules (MIM) for high irradiance photovoltaic energy conversion: a comprehensive review. *Renew Sustain Energy Rev*. 2017;73:477-495.
2. Borden PG. A monolithic series-connected $Al_{0.93}Ga_{0.07}$ as/GaAs solar cell array. *Appl Phys Lett*. 1979;35(7):553-554.
3. Helmers H, Oliva E, Bronner W, Dimroth F, Bett AW. Processing techniques for monolithic interconnection of solar cells at wafer level. *IEEE Trans Electron Dev*. 2010;57(12):3355-3360.
4. Lee JB, Chen Z, Allen MG, Rohatgi A, Arya R. A miniaturized high-voltage solar cell array as an electrostatic MEMS power supply. *J Microelectromechanic Syst*. 1995;4(3):102-108.
5. Wilt D, Wehrer R, Palmisiano M, Wanlass M, Murray C. Monolithic interconnected modules (MIMs) for thermophotovoltaic energy conversion. *Semicond Sci Technol*. 2003;18:209-215.
6. Loeckenhoff R, Dimroth F, Oliva E, et al. Development, characterisation and 1000 suns outdoor tests of GaAs monolithic interconnected module (MIM) receivers. *Prog Photovolt: Res Appl*. 2008;16(2):101-112.
7. Pena R, Algora C, Matías IR, López-Amo M. Fiber-based 205-mW (27% efficiency) power-delivery system for an all-fiber network with opto-electronic sensor units. *Appl Optics*. 1999;38(12):2463-2466.
8. Bottger G, Dreschmann M, Klamouris C, et al. An optically powered video camera link. *IEEE Photon Technol Lett*. 2008;20(1):39-41.
9. Worms K, Klamouris C, Wegh F, et al. Reliable and lightning-safe monitoring of wind turbine rotor blades using optically powered sensors: rotor blade condition monitoring using optically powered sensors. *Wind Energy*. 2017;20(2):345-360.
10. Kimovec R, Topič M. Comparison of measured performance and theoretical limits of GaAs laser power converters under monochromatic light. *Facta Univ - Ser: Electron Energetics*. 2017;30:93-106.
11. Pena R, Algora C, Anton I. GaAs multiple photovoltaic converters with an efficiency of 45% for monochromatic illumination. In: 3rd World Conference on Photovoltaic Energy Conversion (WCPEC) proceedings, Osaka, Japan, 2003, pp. 228–231 Vol. 1.
12. Kimovec R, Helmers H, Bett AW, Topič M. Temperature and injection current dependent electroluminescence for evaluation of single-

junction single-segment GaAs laser power converter. *Informacije MIDEM - J Microelectron, Electron Comp Mater*. 2016;46:142-148.

13. Schubert J, Oliva E, Dimroth F, Guter W, Loeckenhoff R, Bett AW. High-voltage GaAs photovoltaic laser power converters. *IEEE Trans Electron Dev*. 2009;56(2):170-175.
14. Newman FD, Aeby I, Varghese T, Endicter SP, Girard G, Turner MV, Sandoval AC, Fiedor JN, Link SD, Llera-Hurlburt D, et al. Pilot-production yield of indium phosphide-based thermophotovoltaic monolithically interconnected modules. In: 4th World Conference on Photovoltaic Energy Conference (WCPEC) Proceedings, Waikoloa, HI, USA: 2006, pp. 663–666.
15. Ortega P, Bermejo S, Castañer L. High voltage photovoltaic mini-modules. *Prog Photovolt: Res Appl*. 2008;16(5):369-377.
16. Pena R, Algora C. The influence of monolithic series connection on the efficiency of GaAs photovoltaic converters for monochromatic illumination. *IEEE Trans Electron Dev*. 2001;48(2):196-203.
17. Bett AW, Dimroth F, Lockenhoff R, Oliva E, Schubert J. III-V solar cells under monochromatic illumination. In: 33rd IEEE Photovoltaic Specialists Conference proceedings, San Diego, CA, USA: 2008, pp. 362–366.
18. Steiner M, Philipps SP, Hermle M, Bett AW, Dimroth F. Validated front contact grid simulation for GaAs solar cells under concentrated sunlight. *Prog Photovolt: Res Appl*. 2011;19(1):73-83.
19. Espinet-González P, Rey-Stolle I, Algora C, García I. Analysis of the behavior of multijunction solar cells under high irradiance Gaussian light profiles showing chromatic aberration with emphasis on tunnel junction performance. *Prog Photovolt: Res Appl*. 2015;23(6):743-753.
20. Brecl K, Topič M. Simulation of losses in thin-film silicon modules for different configurations and front contacts. *Prog Photovolt: Res Appl*. 2008;16(6):479-488.
21. Wong J. Griddler: intelligent computer aided design of complex solar cell metallization patterns. In: 39th IEEE Photovoltaic Specialists Conference (PVSC) Proceedings, 2013, Tampa, FL, USA, pp. 0933–0938.
22. Pieters BE. A free and open source finite-difference simulation tool for solar modules. In: 40th IEEE Photovoltaic Specialist Conference (PVSC) Proceedings, 2014, Denver, CO, USA, pp. 1370–1375.
23. Ohsawa J, Kawasaki M, Tanaka T, Tsuchida N, Hayakawa S, Yoshida M. A GaAs micro solar cell with output voltage over 20 V. *Jpn J Appl Phys* 1999; 38: 6947–6951, Part 1, No. 12A.
24. Kimovec R, Helmers H, Bett AW, Topič M. On the influence of the photo-induced leakage current in monolithically interconnected modules. *IEEE J Photovolt*. 2018;8(2):541-546.
25. Espinet-González P, Rey-Stolle I, Ochoa M, Algora C, García I, Barrigón E. Analysis of perimeter recombination in the subcells of GaInP/GaAs/Ge triple-junction solar cells. *Prog Photovolt: Res Appl*. 2015;23(7):874-882.
26. Oliva E, Dimroth F, Bett AW. GaAs converters for high power densities of laser illumination. *Prog Photovolt: Res Appl*. 2008;16(4):289-295.
27. Reichmuth SK, Helmers H, Garza CE, Vahle D, de Boer M, Stevens L, Mundus M, Bett AW, Siefer G. Transient I-V measurement set-up for photovoltaic laser power converters under monochromatic irradiance. In: 32nd European Photovoltaic Solar Energy Conference (EU PVSEC) proceedings, Munich, Gemany: 2016, pp. 5–10.
28. Schroder DK. *Semiconductor Material and Device Characterization*. John Wiley & Sons; 2006.
29. Rau U. Reciprocity relation between photovoltaic quantum efficiency and electroluminescent emission of solar cells. *Phys Rev B*. 2007;76:085303(8).
30. Kimovec R, Helmers H, Bett AW, Topič, Marko. Multi-segment photovoltaic laser power converters and their electrical losses. In: 33rd European Photovoltaic Solar Energy Conference and Exhibition (EU PVSEC) proceedings, Amsterdam: 2017, pp. 5–10.
31. Sheldon MT, Eisler CN, Atwater HA. GaAs passivation with Trioctylphosphine sulfide for enhanced solar cell efficiency and durability. *Adv Energy Mater*. 2012;2(3):339-344.
32. Dentai AG, Giles CR, Burrows E, et al. A long-wavelength 10-V optical-to-electrical InGaAs photogenerator. *IEEE Photon Technol Lett*. 1999;11(1):114-116.
33. Walker AW, Hohn O, Micha DN, Blasi B, Bett AW, Dimroth F. Impact of photon recycling on GaAs solar cell designs. *IEEE J Photovolt*. 2015;5(6):1636-1645.
34. Schilling CL, Hohn O, Micha DN, et al. Combining photon recycling and concentrated illumination in a GaAs heterojunction solar cell. *IEEE J Photovolt*. 2018;8(1):348-354.
35. Kayes BM, Nie H, Twist R, Spruytte SG, Reinhardt F, Kizilyalli IC, Higashi GS. 27.6% conversion efficiency, a new record for single-junction solar cells under 1 sun illumination. In: 37th IEEE Photovoltaic Specialists Conference (PVSC) Proceedings, Seattle, WA, USA: 2011, pp. 4–8.
36. Sotoodeh M, Khalid AH, Rezazadeh AA. Empirical low-field mobility model for III–V compounds applicable in device simulation codes. *J Appl Phys*. 2000;87(6):2890-2900.
37. Look DC. The electrical and photoelectronic properties of semi-insulating GaAs. *Semiconductors and Semimetals*, vol. 19, Elsevier; 1983, 75–170, Chapter 2 The Electrical and Photoelectronic Properties of Semi-Insulating GaAs.
38. Levinshtein ME, Rumyantsev SL. Gallium arsenide (GaAs). In: *Handbook Series on Semiconductor Parameters*. World Scientific; 1996:77-103.
39. Luque AL, Viacheslav A. *Concentrator Photovoltaics*. Berlin, Heidelberg: Springer Berlin Heidelberg; 2007.

**How to cite this article:** Kimovec R, Helmers H, Bett AW, Topič M. Comprehensive electrical loss analysis of monolithic interconnected multi-segment laser power converters. *Prog Photovolt Res Appl*. 2018;1–11. https://doi.org/10.1002/pip.3075

## APPENDIX A

**TABLE A1** List of input parameters for the model and respective extraction methods

| Parameter | Value | Description | Extraction Method and Comment |
|---|---|---|---|
| $r_{FINGERS}$ [Ω/□] | 7.83E − 3 | Sheet resistance of grid fingers. | Calculated from a measured resistance of the test structure manufactured on the same wafer as the studied MIM LPC, the test structure width and length, and cross section of the finger. |
| $r_{BUSBAR}$ [Ω/□] | 3.92E − 3 | Sheet resistance of busbars. | Same as finger. Note that the busbar value is 2 times lower, since fingers have trapezoidal cross section and consequently a smaller cross-sectional area. |
| $r_{CONTACT}$ [Ω cm$^2$] | 6.42E − 5 | Specific contact resistance between front metallization and window. | Measured with a transmission line method on dedicated test structures manufactured on the same wafer as the studied MIM LPC. |
| $r_{WINDOW}$ [Ω/□] | 69.1 | Sheet resistance of window plus emitter layers. | Measured with a transmission line method on dedicated test structures manufactured on the same wafer as the studied MIM LPC. |
| $r_{VERTICAL}$ [Ω cm$^2$] | 2.26E − 4 | Combined area-weighted resistance of epitaxial layers for a vertical current flow through the semiconductor epitaxial stack. | Calculated based on a nominal doping and layers thicknesses and literature values for the mobility of majority carriers in the different materials.[36] This is included in the distributed model as a series resistance in the two-diode electrical model. |
| $r_{LCL}$[Ω/□] | 3.28 | Sheet resistance of the lateral conduction layer. | Measured with a transmission line method on dedicated test structures manufactured on the same wafer as the studied MIM LPC. |
| $r_{S.I.\text{-}GaAs}$ [Ω/□] (max–min) | 1.52E6–4.05E4 | Resistivity of a semi-insulating GaAs substrate under illumination (lowest – highest irradiance). | The sheet resistance of a semi-insulating GaAs substrate in the mesa areas where the substrate is exposed to impinging light.[24] Obtained iteratively, for each irradiance separately, by fitting the modeled slope of the *J-V* curve to the measured *J-V* curve at $J_{SC}$, until an agreement between simulations results and measurements was reached (a relative difference in the slope of the measured and simulated illuminated *J-V* curves at $J_{SC}$ is below 2%). |
| $r_{S.I.\text{-}GaAs\text{-}dark}$ [Ω/□] | 1E8 | Resistivity of a semi-insulating GaAs substrate in the dark. | Literature value.[37] |
| $r_{SH}$ [Ω cm$^2$] | 3.5E6 | Area-weighted shunt resistance connected in parallel to the two-diode electrical PV model. | Extracted from the measured dark *J-V* curve in reverse voltage region. |
| $n_1$ | 1 | Ideality factor for the first diode in two-diode PV model (neutral region). | Preset. |
| $n_{2b}$ | 2 | Ideality factor for the second diode in two-diode PV model (depletion zone). | Preset. |
| $n_{2p}$ | 2 | Ideality factor for the second diode in two-diode PV model (perimeter). | Preset. |
| $J_{01}$ [A/cm$^2$] | 5E − 20 | Saturation current density for the first diode in two-diode PV model (neutral region). | Fitted to $J_{sc}$-$V_{oc}$ pairs from illuminated *J-V* measurements data point at high irradiances (48.1 to 83.1 W/cm$^2$ at $\lambda_0$ = 809 nm). |
| $J_{02}$ [A/cm$^2$] | 4E − 11 | Saturation current density for the second diode in two-diode PV model (depletion zone + perimeter recombination). | Extracted from the measured dark *J-V* curve at forward bias at medium voltages (5.3-6.3 V). |
| $J_{02b}$ [A/cm$^2$] | 2E − 11 | Bulk component of the saturation current density for the second diode in two-diode PV model (depletion zone). | Literature value.[18] |
| $J_{02p}$ [A/cm] | 5E − 12 | Perimeter component of the saturation current density for the second diode in two-diode PV model (perimeter recombination). | Calculated from $J_{02}$, $J_{02b}$, area of the *pn*-junction and perimeter of the *pn*-junction using Equation (1). (perimeter/area ratio of the studied device (P/A = 57 cm$^{-1}$)). |
| $E_g$ [eV] | 1.42 | Bandgap of GaAs at 300 K | Literature value.[38] |
| *SR* [A/W] | 0.54 | Spectral response at $\lambda_0$ = 809 nm | Measured with a double-monochromator[39] on a specific test cell with conventional PV cell architecture manufactured on the same wafer and corrected for grid shading of the actual sample. |

**TABLE A2** Summary of resistive and shunting power losses related to different components for three considered monochromatic irradiances: $G_{low}$ = 1.8 W/cm$^2$, $G_{optimal}$ = 13.2 W/cm$^2$, and $G_{high}$ = 83.1 W/cm$^2$

| Case [Low/Optimal/High Irradiance] | $P_{mpp}$ [mW] | | | Relative power loss $\Delta P/P_{mpp}$ [%] | | |
|---|---|---|---|---|---|---|
| All resistive losses excluded ("reference case") | 30.2 | 242.3 | 1647.1 | | | |
| $r_{BUSBAR}$, $r_{FINGERS}$ | 30.2 | 242.3 | 1644.9 | 0.0 | 0.0 | 0.1 |
| $r_{CONTACT}$ | 30.2 | 241.8 | 1627.0 | 0.0 | 0.2 | 1.2 |
| $r_{WINDOW}$ | 30.2 | 241.8 | 1624.3 | 0.0 | 0.2 | 1.4 |
| $r_{VERTICAL}$ | 30.2 | 242.0 | 1640.3 | 0.0 | 0.1 | 0.4 |
| $r_{LCL}$ | 30.1 | 235.2 | 1267.7 | 0.3 | 3.0 | 29.9 |
| $r_{SI\text{-}GaAs}$ | 29.2 | 236.8 | 1593.9 | 3.4 | 2.3 | 3.3 |
| $r_{SH}$ | 30.2 | 242.3 | 1647.1 | 0.0 | 0.0 | 0.0 |
| All resistive losses included | 29.1 | 228.5 | 1162.6 | 3.8 | 5.9 | 36.5 |

**TABLE A3** Summary of recombination losses of the investigated device compared with the assumed "best" case scenario related to different recombination regions for the three considered irradiances: $G_{low}$ = 1.8 W/cm$^2$, $G_{optimal}$ = 13.2 W/cm$^2$, and $G_{high}$ = 83.1 W/cm$^2$. Note that due to the applied procedure to determine separate components of $J_{02}$ in the model, the nominal $J_{02b}$ in our model was already set to the state-of-the-art value; therefore, losses in this case are 0

| Case [Low/Optimal/High Irradiance] | $P_{mpp}$ [mW] | | | Relative Power Loss $\Delta P/P_{mpp}$ [%] | | |
|---|---|---|---|---|---|---|
| "Best" case (iv) (grey diamonds in Figure 11) | 32.4 | 244.1 | 1184.7 | | | |
| $J_{01}$ | 32.2 | 241.5 | 1166.9 | 0.6 | 1.1 | **1.5** |
| $J_{02b}$ | 32.4 | 244.1 | 1184.7 | 0.0 | 0.0 | **0.0** |
| $J_{02p}$ | 29.1 | 228.6 | 1168.7 | 10.2 | 6.3 | **1.4** |
| All recombination losses included | 28.9 | 226 | 1162.6 | 10.8 | 7.4 | **2.9** |